




Realization of exchange bias control with manipulation of interfacial frustration in magnetic complex oxide heterostructures

Ji Zhang ^{1,2,*}, Jack Yang,^{1,2} Grace L. Causer,² Junjie Shi,¹ Frank Klose,² Jing-Kai Huang,¹ Allen Tseng ¹,
Danyang Wang ¹, Xiaotao Zu,³ Liang Qiao,^{3,†} Anh Pham,^{1,4,‡} and Sean Li^{1,§}

¹*Materials and Manufacturing Futures Institute, School of Materials Science and Engineering, University of New South Wales, Sydney, New South Wales 2052, Australia*

²*Australian Nuclear Science and Technology Organisation, Lucas Heights, New South Wales 2234, Australia*

³*School of Physics, University of Electronic Science and Technology of China, Chengdu 610054, China*

⁴*Center for Nanophase Materials Sciences, Oak Ridge National Laboratory, Oak Ridge, Tennessee 37831, USA*



(Received 18 June 2021; revised 10 September 2021; accepted 15 November 2021; published 30 November 2021)

Rich exchange bias (EB) behaviors were previously observed when ferromagnetic (FM) materials contacted a spin glass, demonstrating magnetic degrees of freedom of the coupling between the glass and FM spins. However, the correlation between the degree of magnetic spin frustration and the strength of the resulting EB is far from being understood. Here, we systematically investigate the dependency of EB on interfacial spin frustration in magnetic complex oxide heterostructures including $\text{La}_{0.7}\text{Ca}_{0.3}\text{MnO}_3/\text{CaMnO}_3$ (LCMO/CMO) systems. The experimental analysis revealed that the extent of interfacial spin frustration is determined by the subtle competition between different types of magnetic orders related to the glassy spin behaviors at the interface. Such spin frustration can be manipulated through strain engineering through changes in the Mn e_g orbital by alternating the stacking sequence of the heterostructures. A highly tunable EB field with 95% change of strength between the highly and weakly frustrated heterostructures has been achieved. Magnetic depth profiles of the heterostructures provide convincing evidence that a magnetically depressed region always occurs in the LCMO layer at the LCMO/CMO interfaces irrespective of the stacking sequence. Finally, EB is established at the magnetic interface in the LCMO layer.

DOI: [10.1103/PhysRevB.104.174444](https://doi.org/10.1103/PhysRevB.104.174444)

I. INTRODUCTION

Exchange bias (EB) is a physical phenomenon of the exchange interaction between an antiferromagnet (AFM) and a ferromagnet (FM) at their interface. It has been widely used to stabilize the magnetization of soft FM layers from the influence of thermal fluctuation to reduce magnetic noise for maximizing the sensitivity of the magnetic sensors [1,2]. This phenomenon is particularly important for nonvolatile magnetic memories. While microelectronic devices continue to diminish in size to achieve better performance, controlling the EB has become more prominent because of the energy loss and heat dissipation caused by passing the signals from one transistor to the next. With the limits of magnetic domain miniaturization in sight, there has been an enormous drive to radically innovate materials and technologies to overcome the fundamental limit of magnetic coupling associated with the thermal fluctuation to embrace the era of massive information/data explosion for the data-centric computing paradigm.

In general, an externally applied magnetic field has very limited influence on the spin orientation of AFMs, resulting in

a very small or no net magnetization. When a soft FM material is strongly exchange-coupled to an AFM, an interfacial spin pinning effect is induced, also known as EB. This pinning effect manifests as a horizontal shift of the magnetic hysteresis ($M-H$) loop along the magnetic field axis. It enhances the coercivity when the material is cooled below the blocking temperature (T_B) under a static magnetic field. In the case that interfacial spins are colinearly aligned, FM coupled interfacial spin [Fig. 1(a)] results in a negative EB, i.e., a left-shifted $M-H$ loop [1], while a positive EB is achieved as a result of AFM coupled interfacial spins [Fig. 1(b)] [3]. However, interfacial spin configurations can be far more complicated in the case of noncolinearly aligned interface spins [Fig. 1(c)] [4]. It is demonstrated that the EB direction changes from negative to positive as the cooling field is enhanced. In addition, the role of frustration in EB systems is highlighted using a FM and canonical spin-glass (SG) bilayer [5], and it is suggested that the exchange coupling exists randomly at the bilayer interface, as illustrated in Fig. 1(d). It is also suggested that the existence of frustration is consistent with the existence of EB, and strong frustration supports a large EB. Further, the experimental results on a FM coupled to a SG provide a direction for studies of EB and possibilities for manipulation of internal magnetic degrees of freedom.

Frustration is a common phenomenon in nature and often exists as disorder or impurities in ordered systems. In magnetic materials, frustration is induced by strong, short-range

*ji.zhang1@unsw.edu.au

†liang.qiao@uestc.edu.cn

‡phamad@ornl.gov

§sean.li@unsw.edu.au

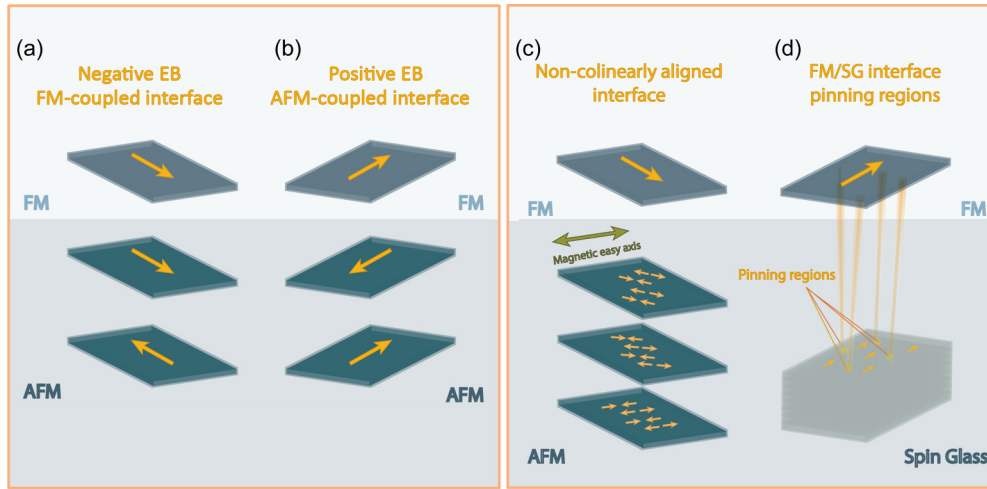


FIG. 1. Schematic diagrams of the interfacial spin alignments of exchange biased multilayers, depicting the collinearly aligned (a) ferromagnetic (FM)-coupled and (b) antiferromagnetic (AFM)-coupled interfaces, and the (c) noncollinearly aligned and (d) FM/spin-glass (SG) interfaces resulting in an interfacial domain state and random pinning regions, respectively.

magnetic interactions which disrupt the long-range magnetic order, leading to unexpected properties and magnetic states, such as SGs [6], spin liquids [7], spin ices [8], and skyrmions [9]. Experimental and theoretical studies on these complex spin textures have been extensively carried out, particularly for SGs, due to their fundamental importance [6] and their potential applications in neural information processing [10]. Some pioneering works have observed EB from SGs in alloys and compounds [6], dilute magnetic oxides [11], and nanoparticles [12]. Recent studies on perovskite manganite and cobaltite thin films suggest that SG phases are established at the chemical interfaces through the competition between double-exchange-mediated FM and superexchange-mediated AFM spin orderings [13–15]. It is found that EB is typically strongly correlated with interfacial frustration, indicating that EB is observed only at temperatures below the freezing point of the SG phase [13]. Another less common example of EB in manganites is observed in a magnetically separated but chemically uniform $\text{La}_{2/3}\text{Ca}_{1/3}\text{MnO}_3$ thin film [16,17]. In both examples [16,17], EB is believed to be induced at the nominal interface of a magnetically frustrated layer (i.e., SG) and a FM layer. It was suggested that the existence of frustration is consistent with the existence of EB [5]. A theoretical study suggests that a system with a higher degree of frustration favors greater EB [18]; however, direct experimental evidence of such a relation is still pending. Moreover, the frustration-induced magnetization reduction has a significant effect on the magnetotransport of the FM layer in a magnetic tunneling junction and exchange coupling in a heterostructure [19]. Therefore, understanding and precise control over the interfacial SG properties and magnetization dynamics of frustrated perovskite manganite heterostructures are of vital importance.

In this paper, we focus on controlling the EB by manipulating the glassy spin behaviors at the $\text{La}_{0.7}\text{Ca}_{0.3}\text{MnO}_3/\text{CaMnO}_3$ (LCMO/CMO) interface by manipulating the interfacial strain. The raised glassy spin is due to the frustration at the nominal interface between the FM and the G-type AFM [13]. It is well established that strain-induced Jahn-Teller

distortions and octahedral tilting in perovskite manganites can significantly modify the orbital couplings of MnO_6 octahedra, leading to a shift in the relative spin density states of Mn ions and resulting in rich phase diagrams for the manganites [20]. This suggests that strain engineering is a viable route to control the degree of magnetic spin frustration at the LCMO/CMO interface, which consequentially determines the EB strength [21]. This is achieved in this paper by changing the stacking sequences of LCMO and CMO layers deposited onto (001)-oriented SrTiO_3 (STO) substrates. Compressive strain (Type C) is introduced into the LCMO layer through a stacking sequence of LCMO(CMO(relaxed))/STO, while tensile strain (Type T) is introduced into the LCMO layer to form the heterostructure with a stacking sequence of CMO(relaxed)/LCMO/STO. Volume-averaged magnetic measurements reveal that the heterostructure under compressive strain displays greater spin frustration than the heterostructure under tensile strain. In addition, an enhanced EB effect is found in the heterostructure with a higher degree of spin frustration induced by the compressive strength. Going beyond volume-averaged magnetic measurements (which was the only type of magnetic data examined in prior studies [13,22,23]), we obtain detailed magnetic depth profiles of the heterostructures using polarized neutron reflectometry (PNR). This enables us to reveal the spatial spin configurations at the different LCMO/CMO interfaces of the two heterostructures, from which the fundamental physics of EB induced by interfacial spin frustration is consolidated.

II. METHODS

Pulsed-laser deposition with a KrF excimer laser ($\lambda = 248$ nm) and *in situ* reflective high-energy electron diffraction were used to fabricate the LCMO/CMO heterostructures [24]. The films were deposited on TiO_2 -terminated (001)-oriented STO substrates. Two heterostructures were grown comprised of an LCMO (24 nm)/CMO (47 nm)/STO structure and a CMO (45 nm)/LCMO (25 nm)/STO structure denoted as Type-C and Type-T

heterostructures, respectively. The thicknesses of the LCMO and CMO layers in both heterostructures are intentionally retained as similar as possible. Both heterostructures were prepared under the identical deposition conditions, i.e., a laser energy density of 1.7 J/cm^2 at a frequency of 2 Hz and a chamber base pressure of 10^{-8} Torr, with a substrate temperature of 800°C and a 100 mTorr oxygen partial pressure. After deposition, each heterostructure was allowed to be cooled down to room temperature at a ramp rate of 20°C/min with the same oxygen partial pressure.

The layer structure, layer thicknesses, and lattice strain of each heterostructure were characterized by x-ray diffractometry (XRD), x-ray reflectivity (XRR), and x-ray reciprocal space mapping (RSM), respectively. Magnetic properties were measured using a superconducting quantum interference device magnetometer with an in-plane magnetic field applied parallel to the STO (100) direction. Magnetic hysteresis ($M-H$) loops were measured after field cooling (FC) in a set of selected cooling fields H_{cf} . During the $M-H$ measurements, the measuring field was swept between ± 40 kOe, ensuring that all spins were aligned with the field to minimize the possibility of measuring minor $M-H$ loops. The temperature-dependent magnetization ($M-T$) was measured during the warming process after FC and zero-field-cooling (ZFC) processes under a set of selected magnetic fields. The EB field (H_E), which results in the horizontal shift of the $M-H$ loops along the field direction, is defined as $H_E = (H_+ + H_-)/2$, and the coercivity H_C is defined as $H_C = (H_+ - H_-)/2$, where H_+ and H_- are the right and left coercivity fields, respectively. The shift of the $M-H$ loop along the magnetization direction denoted as M_E is defined as $M_E = (M_+ + M_-)/2$, where M_+ and M_- are the positive and negative remnant magnetization, respectively. Magnetization relaxation [$M(t)$] was measured to examine the spin dynamics of the heterostructures.

Magnetic memory measurements were carried out by positive ($T_1 - T_2 - T_1$) and negative ($T_2 - T_1 - T_2$) temperature cycles (T cycles) with $T_2 > T_1$. Both positive and negative T cycles were performed after FC/ZFC protocols. Within a negative T cycle, the heterostructures were cooled by FC (ZFC) protocols from 300 to 50 K, and then the magnetic field was changed to 0 Oe (300 Oe) with respect to the cooling protocols. Then $M(t)$ measurements were carried out. Upon the completion of the first $M(t)$ measurement, the temperature was decreased to 10 K without changing the magnetic field to measure the second $M(t)$ datum. Subsequently, the temperature was increased back to 50 K, and the last $M(t)$ dataset was measured. In contrast, for the positive T cycle, the temperature was decreased from 300 to 10 K for the first $M(t)$ measurement and then raised up to 50 K for the second measurement and finally decreased back to 10 K for the last measurement.

PNR measurements were carried out using the time-of-flight instrument PLATYPUS located at Australian Nuclear Science and Technology Organization (ANSTO). PNR is a technique capable of accurately determining the magnetic and chemical depth profiles of heterostructure thin films [25]. PNR measures the reflectivity of a neutron beam at small scattering angles as a function of the scattering vector (\mathbf{Q}). For a specular reflected neutron beam, \mathbf{Q} is directed perpen-

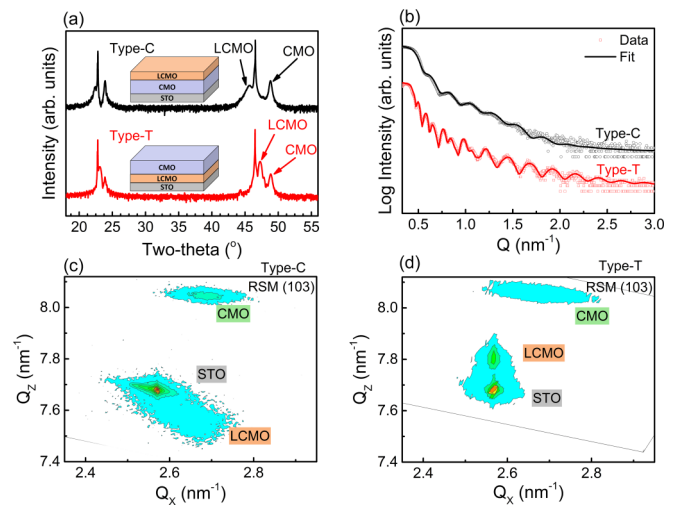


FIG. 2. (a) X-ray diffraction, and (b) x-ray reflectivity data of the Type-C and Type-T heterostructures. Reciprocal space mapping (RSM) of the asymmetric lattice point around the (103) reflection of the SrTiO₃ (STO) substrate is shown for the (c) Type-C and (d) Type-T heterostructures.

dicularly to the surface of the heterostructure. By analyzing the PNR data, a model consisting of the depth-dependent scattering length density (SLD) profile can be obtained. The SLD profile comprises the nuclear and magnetic SLDs of the heterostructure which are related to the chemical composition and magnetization of the materials in the sample, respectively. The neutron scattering lengths relevant to this paper are [26] Sr: 7.02×10^{-6} nm, Ti: -3.44×10^{-6} nm, O: 5.803×10^{-6} nm, Mn: -3.73×10^{-6} nm, La: 8.244×10^{-6} nm, and Ca: 4.70×10^{-6} nm. PNR data were obtained for two neutron spin cross-sections, namely, R^{++} , and R^{-} . Here, the + and - signs represent the polarization of the neutron spin, i.e., either spin up or spin down. The reflectivity difference between R^{++} and R^{-} channels provides information about the component of the in-plane magnetization parallel to the measurement field, in which the depth dependence of the magnetization is encoded in the scattering vector (\mathbf{Q}).

III. RESULTS AND DISCUSSIONS

A. Correlation of stacking sequence and states of strain

Firstly, we demonstrate that epitaxial strains of LCMO can be manipulated by the stacking sequence of a heterostructure while minimizing the influence from the substrate. The pseudocubic lattice parameter of bulk LCMO and CMO are 0.386 nm [27] and 0.375 nm [28], respectively. We use a relatively thick CMO (45 nm) to ensure full strain relaxation in both Type-C (LCMO/CMO/STO) and Type-T (CMO/LCMO/STO) heterostructures. When grown on top of a fully relaxed CMO lattice (lattice constant ~ 0.375 nm), LCMO shows an in-plane compressive strain state, while it experiences an in-plane tensile strain state when grown on top of an STO substrate (lattice parameter of 0.390 nm), as revealed by XRD. Figure 2(a) shows the θ - 2θ spectra of the Type-C and Type-T heterostructures, measured with respect to the surface normal. For the Type-C heterostructure, the LCMO (002)

reflection is located at the left of the STO (002) reflection. In comparison, the LCMO (002) reflection is located at the right of the STO (002) reflection in the Type-T heterostructure. This indicates the Type-C and Type-T heterostructures are subject to tensile and compressive strains, respectively. The occurrence of lattice strain relaxation in both heterostructures is further verified through the RSM of the (103) planes, as shown in Figs. 2(c) and 2(d). Figure 2(b) shows the XRR data of each heterostructure, overlaid with best fit profiles. The presence of persistent thickness fringes (up to $Q = 3 \text{ nm}^{-1}$) indicate the high quality of both interfaces. The fitted layer thicknesses were also confirmed with cross-section transmission electron microscopy images shown in Fig. S1 in the Supplemental Material [29] (see also Refs. [27,28] therein). The extracted lattice parameters and individual layer thicknesses for both films are shown in Table S1 in the Supplemental Material [29]. It is found that the lattice of the CMO layer in both heterostructures is relaxed, as the critical thickness of CMO on STO is $\sim 10 \text{ nm}$ [30], as determined by classic Matthews-Blakeslee or People-Bean models [31,32]. As a result, the out-of-plane and in-plane lattice parameters of the CMO layers are like that of the bulk lattice parameter of 0.375 nm for the pseudocubic structure [28]. On the other hand, the lattice parameters of the LCMO layers (0.386 nm in the bulk pseudocubic phase [27]) are dependent on the stacking sequence of the heterostructure. The c/a ratios of 0.97 and 1.03 are obtained for the CMO (45 nm)/LCMO (25 nm)/STO and LCMO (24 nm)/CMO (47 nm)/STO heterostructures, verifying that they are in compressive (Type-C) and tensile (Type-T) strain states, respectively, which is like other oxide heterostructures [17,33,34]. This provides us the foundation to investigate the interactions between strains and spin frustrations in complex oxide heterostructures as detailed below.

B. EB and glassy spins

Magnetic hysteresis ($M-H$) loops shown in Figs. 3(a) and 3(b) for the Type-C and Type-T heterostructures demonstrate that EB is induced by the strained interfaces. When a small cooling field ($H_{cf} = 150 \text{ Oe}$) is applied during the cooling process, the negative coercive field (H_-) is shifted to the left, while the positive coercive field (H_+) remains almost unchanged. Furthermore, the stacking sequence significantly affects the shape of the hysteresis loops. While the Type-T heterostructure shows a sharp magnetic reversal with a smaller coercivity (H_C), the Type-C heterostructure shows a relatively slow magnetic reversal response with a much larger H_C .

The presence of EB in both Type-C and Type-T heterostructures may be attributed to the presence of glassy spins therein. Figures 3(c) and 3(d) plot the magnetic field dependence of the $M-T$ (temperature) behaviors for the Type-C and Type-T heterostructures, respectively. The paramagnetic-to-FM transition temperature (Curie temperature, T_C) is determined using $M-T$ curves measured at 50 Oe for both the Type-C ($T_C \approx 155 \text{ K}$) and Type-T ($T_C \approx 147 \text{ K}$) heterostructures. As expected, the bulk Curie temperature ($T_C \approx 250 \text{ K}$) is higher than both heterostructures due to straining exerted on the LCMO layer. It is attributed to Jahn-Teller distortion causing the splitting of the twofold e_g degenerated states from Mn, consequentially weakening the double-exchange

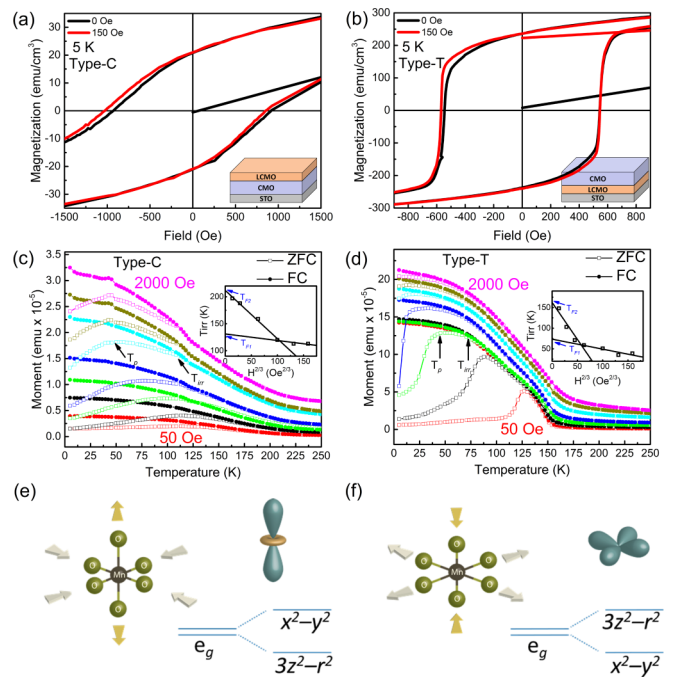


FIG. 3. $M-H$ data (enlarged view) of the (a) Type-C and (b) Type-T heterostructures after zero-field cooling (ZFC; 0 Oe) and field cooling (FC; 150 Oe) procedures. $M-T$ data of the (c) Type-C and (d) Type-T heterostructures after ZFC and FC procedures in a range of measurement fields between 50 and 2000 Oe . The inset shows the corresponding $H^{2/3}$ vs T_{irr} plots, where the fitting (line) to the data (dot) is obtained using Eq. (1). Schematic representation of the MnO_6 octahedral distortions influenced by (e) compressive strain and (f) tensile strain and subsequent energy degeneration of $\text{Mn}^{3+} e_g$ subbands.

coupling [35]. Moreover, features are observed in the $M-T$ curves which include a maximum temperature (T_P) with a cusp shaped ZFC magnetization and a bifurcation between the FC and ZFC curves defined as the irreversible temperature (T_{irr}). The existence of T_P and T_{irr} has been reported in different magnetic systems, such as superparamagnetic and frustrated magnetic interactions like SG and spin-cluster systems [36]. In this paper, superparamagnetism can be excluded due to the lack of monotonous increase behavior for FC magnetization when lowering the temperature. As expected, both T_{irr} and T_P shift to lower temperatures with increasing field, indicating spin freezing is suppressed by the applied magnetic fields. Furthermore, both T_P and T_{irr} for the Type-T heterostructure respond faster (slopes of the inset in Fig. 3) to the increased field than those in the Type-C heterostructure, indicating stronger spin frustration in the latter.

Different degrees of magnetic frustration originate from the subtle competition among several types of magnetic orderings. These include the interfacial superexchange and double exchange at the interface [13], octahedral distortion-induced orbital degeneracy in LCMO favors an AFM superexchange, which competes with the native FM double-exchange interactions [37], and the coupling of degenerate orbital states across interfaces [38]. In our case, the degree of frustration reflects the total contributions from the ordering competitions, which is closely related to the lattice strain of the heterostructure.

For the Type-C heterostructure, elongation of the LCMO lattice along the out-of-plane direction would potentially lower the energy level of $3z^2 - r^2$ orbitals in e_g subbands [39,40], as demonstrated in Fig. 3(e), which can further weaken the FM coupling along the in-plane direction. This strain effect would lead to the strong reduction of magnetization observed in the Type-C heterostructure. While for the Type-T heterostructure, the $x^2 - y^2$ orbital in e_g subbands is favored as expected from a shrinkage of the LCMO lattice along the out-of-plane direction [39,40], as demonstrated in Fig. 3(f). As observed in Type T, a higher magnetization along in-plane direction is observed. Consequently, the Type-C heterostructure as expected has stronger interfacial coupling across the LCMO/CMO interface than the Type-T heterostructure, as illustrated in Figs. 3(e) and 3(f), the $3z^2 - r^2$ orbitals would have more overlapping with neighboring O $2p$ orbitals than the $x^2 - y^2$ orbitals. Therefore, Type C is expected to show a strong interfacial coupling and a strong competition between the AFM and FM orderings. However, weaker interfacial coupling is expected for the Type-T case as overlapping of the $x^2 - y^2$ orbitals across the LCMO/CMO interface is very minimum. To fully understand the interfacial magnetism of the LCMO/CMO interfaces, further quantitative investigation of the orbital states of Mn ions is required. However, this is beyond the scope of this paper.

To better understand the glassy magnetic characteristics of the Type-C and Type-T heterostructures, T_{irr} as a function of the applied magnetic field were fitted using the Almeida-Thouless equation based on the Sherrington-Kirkpatrick model (mean field theory of SG) [41]:

$$H(T_{\text{irr}})^{2/3} \propto \frac{1 - T_{\text{irr}}}{\Delta J}, \quad (1)$$

where $H(T_{\text{irr}})$ is the applied magnetic field, ΔJ is the width of the distribution of the exchange energy interaction, and T_F is the zero-field freezing temperature below which spins are ‘‘frozen’’ in each orientation. The fitting results are shown as insets in Figs. 3(c) and 3(d) for the Type-C and Type-T heterostructures, respectively. The data can be fitted by Eq. (1) for two distinct magnetic field regimes which yield two T_F for each heterostructure. This result indicates that our system is not Ising type in the mean field theory of SG since a linear fit to the results is not possible [42]. Similar results have also been observed in strained BiFeO₃ thin films [43], where the observed crossover region in the T_{irr} vs $H^{2/3}$ plot was thought to be coupled with some long-range order interactions, i.e., strain.

C. Magnetic relaxation

Up to here, both EB effect and glassy spin behaviors are present in the LCMO/CMO heterostructures. Generally, in systems with glassy spins, the dynamic relaxation of the magnetization and memory effect (detailed in Sec. 4 in the Supplemental Material [29]; see also Refs. [28,36,42,44–47] therein) is expected [6]. The spin dynamics of the heterostructures are measured to acquire the time-dependent magnetic moment data $M(t)$ at the selected temperatures to further consolidate the glassy nature of the heterostructures. Both heterostructures were cooled to the selected temperature

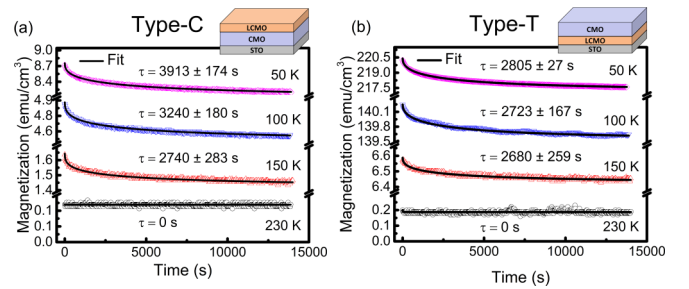


FIG. 4. Magnetic relaxation data of the (a) Type-C and (b) Type-T heterostructures after field cooling (FC) measured at various temperatures. The measured data (dots) are fit (lines) using the standard stretched exponential function of Eq. (2).

under a cooling field of $H_{\text{cf}} = 300$ Oe. The magnetic field was switched off after waiting for 600 s. Subsequently, the $M(t)$ signals were measured. The measurement results are shown in Figs. 4(a) and 4(b) for Type-C and Type-T heterostructures, respectively, wherein the data were fitted using the standard stretched exponential function:

$$M(t) = M_0 + M_g \exp\left[-\left(\frac{t}{\tau}\right)^{1-n}\right], \quad (2)$$

where M_0 and M_g are the magnetization of the intrinsic FM and glassy components, respectively. Here, τ is a characteristic relaxation time constant, and n is a stretching exponent which has a value between 0 and 1. For $n = 1$, there is no relaxation of the system, whereas when $n = 0$, the system has a uniform energy barrier with an exponential relaxation of $M(t)$, which relaxes with a single time constant. Fitting the $M(t)$ data measured at temperatures $T < 230$ K yields a value of n between 0.5 and 0.6 for both heterostructures (for detailed fitting results see Fig. S2 in the Supplemental Material [29]), which is typical for SG systems [48]. In addition, the value of τ for both Type-C and Type-T heterostructures increases with decreasing temperature, which is also the characteristic behavior of a SG system [49]. Again, the fitted results indicating a stronger frustration are present in the Type-C heterostructure, as the value of τ is always larger than the Type-T heterostructure.

D. Correlation of glassy spins and EB

The above results show that different degrees of spin frustrations in CMO/LCMO heterostructures are controllable by the epitaxial strains, which subsequently lead to the observed EB phenomena in these heterostructures. It is believed that external parameters such as cooling field strength and temperature can also regulate the degree of spin frustration. Here, we demonstrate that EB can be manipulated through controlling the applied magnetic field and temperature, revealing the operating conditions under which EB can be harnessed in real device applications. Similar experiments have also been reported on SG/FM bilayers [50] and FM/G-type AFM perovskite heterostructures [22]. A wide range of cooling fields from 0 to +40 kOe were used for the $M-H$ loop measurements at 5 K, as shown in Figs. 5(a) and 5(b) for Type-C and Type-T heterostructures, respectively. Both heterostructures

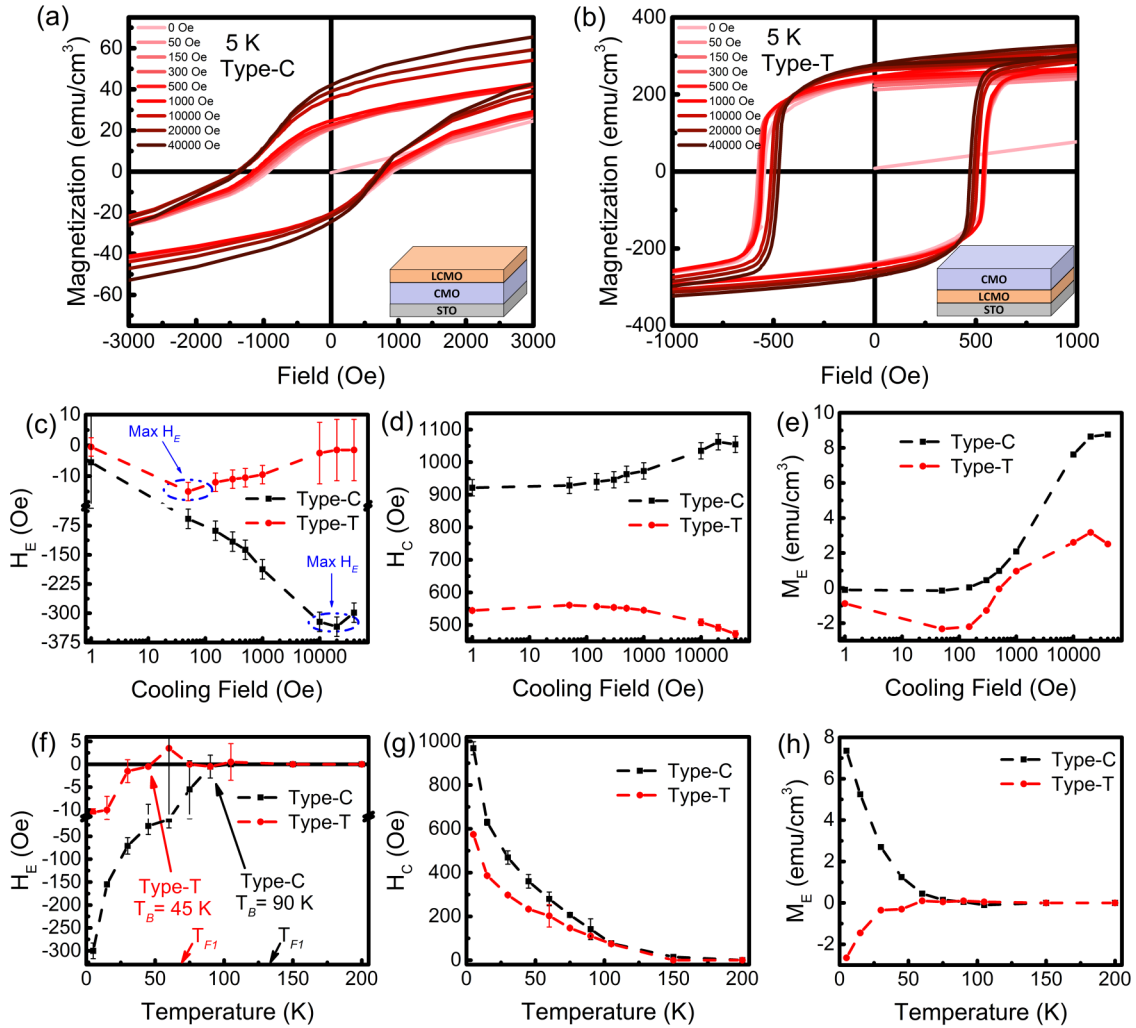


FIG. 5. The H_{cf} -dependent $M-H$ loops of the (a) Type-C and (b) Type-T heterostructures. The values of (c) H_E , (d) H_C , and (e) M_E as a function of H_{cf} are also plotted. Note that zero-field cooling (ZFC) results are displayed as $H_{cf} = 1$ Oe since the x axis is plotted on a log scale. The (f) H_E , (g) H_C , and (h) M_E as a function of temperature are also shown.

exhibit a smaller volume-averaged saturation magnetization (M_S) of 103 emu/cm³ for Type C and 430 emu/cm³ for Type T, as compared with theoretical magnetization of LCMO [596 emu/cm³ (3.7 μ_B /u.c.)]. The reduction of M_S has previously been observed in strained La_{0.7}Ca_{0.3}MnO₃ films [35]; it is attributed to the octahedral distortion of the LCMO lattice, causing the degeneracy of the e_g orbital to be lifted, which weakens the double-exchange interaction [35], as we have discussed earlier, while the strongly reduced M_S of the Type-C heterostructure is related to factors such as lattice defects (see Fig. S1(f) in the Supplemental Material [29]) and enhanced interfacial spin frustration [discussed later in Fig. 7(d)].

Figures 5(c)–5(e) plot the cooling field-dependent H_E , H_C , and M_E , respectively, for both heterostructures. The evolution of H_E shows dramatically different behaviors between the two heterostructures. The Type-T heterostructure exhibits a maximum $H_E = -15$ Oe in a very low H_{cf} of 50 Oe, and it reaches zero in H_{cf} of 10 kOe, while the Type-C heterostructure shows a continuous increase of H_E with H_{cf} up to the critical value of 20 kOe, showing the maximum biased field of -334 Oe. Subsequently, the magnitude of H_E starts to decrease with

further increasing H_{cf} [see Fig. 5(c)]. Likewise, H_C maximizes at the critical H_{cf} value, which corresponds to Type C and Type T, respectively, followed by the reduction of H_C with further increasing H_{cf} . The increase of H_C is expected because the FM spins are exchange coupled with the frustrated spins; thus, extra magnetic field is required to reverse the exchange coupled FM spins. The observed critical H_{cf} suggest a direct correlation between the EB and the frustrated spins. The cooling field aligns the FM spins and forces portions of the frustrated spins to become FM coupled. Before the critical H_{cf} , the enhanced EB is predominant due to a better FM spin alignment; while H_{cf} is further increased, the reduced EB caused by the number of frustrated spins is decreased. As shown in Fig. 5(c), there is a large difference between the values of the critical H_{cf} of Type T ($H_{cf} = 50$ Oe) and Type C ($H_{cf} = 20$ kOe) at which the maximum H_E is obtained. This result reflects the degree of frustration of the glassy region, where a higher degree of frustration results in a larger H_E [21]. Direct proof is seen in the PNR results, which is included in the following section. For the less frustrated Type-T heterostructure, a small cooling field can transfer the glassy spin

phase into a predominantly FM ordered state (i.e., the field is large enough to align with the majority of spins), which lowers the amount of overall exchange coupled spins, while switching to the predominantly FM ordered state requires a much larger magnetic field for the strong frustrated Type-C heterostructure. Moreover, as shown in Figs. 5(a) and 5(b), both heterostructures show vertical shifts in the magnetization axis, e.g., M_E , which increases with increasing H_{cf} . This behavior in M_E with cooling field is believed to be related to the competition among different energies at the interface of the FM domains and the glassy spin domains [51]. According to the scenario of Tang *et al.* [51], these competing energies include (i) the Zeeman energy (E_Z), (ii) the anisotropy energy of the FM domain (E_F), (iii) the anisotropy energy of the glassy spin domain (E_{GS}), and (iv) the exchange energy at the FM/SG interface (E_{int}). When $|-E_Z + E_F| < |E_{int}|$ and $|-E_Z + E_F| < |E_{GS}|$, a positive M_E results because the effective Zeeman energy $|-E_Z + E_F|$ is too weak to overcome the interfacial energy barrier or to rotate the glassy spins. Consequentially, portions of FM spins remain pinned, leading to a vertical shift of the magnetization axis. Similar positive shifts of $M-H$ loops along the M axis have also been observed in SG perovskite cobaltite [51] and in LCMO/STO thin films [16]. In the case of the Type-T heterostructure, the overall trend of increasing M_E with H_{cf} can also be explained using the above competing energy mechanism. However, the reason for the observed negative M_E in the Type-T heterostructure is still unclear.

To understand the temperature effects on the EB behaviors, i.e., blocking temperature (T_B), $M-H$ loop results measured at elevated temperatures after FC processes were performed (Fig. S4 in the Supplemental Material [29]), as shown in Figs. 5(f)–5(h). Both magnitudes of H_E and H_C decrease as the temperature increases because the interfacial exchange energy is weakened. The characteristic T_B is determined when $H_E = 0$. By extrapolating the H_E-T plots [Fig. 5(f)], it is found that $T_B = 90$ and 45 K for the Type-C and Type-T heterostructures, respectively. The T_B is lower than the Néel temperature of bulk CMO and just below the T_f of the glassy spins, indicating that spin freezing play an important role in enhancing the EB effect. Similarly, M_E reaches zero at T_B as well. In addition, the value of H_C reduces to zero when the temperature nears the T_C of each heterostructure.

E. PNR: Magnetic depth profiles

The magnetic measurements performed above can only provide us with a volume-averaged magnetic behavior of CMO/LCMO heterostructures; it cannot provide us the locations of the spin frustration regions in these heterostructures at atomic scale with the corresponding degree of spin frustration. To overcome these limitations, PNR measurements were conducted to establish the magnetic depth profiles for these heterostructures. Figure 6(a) shows the experimental setup used for the PNR measurements. Figures 6(b) and 6(c) plot the PNR R^{++} and R^{--} reflectivity patterns (top panel) and the corresponding neutron spin asymmetry data (bottom panel), defined by $(R^{++} - R^{--})/(R^{++} + R^{--})$, of Type-C and Type-T heterostructures, respectively. Experimental data were obtained at 6.1 K after FC in the presence

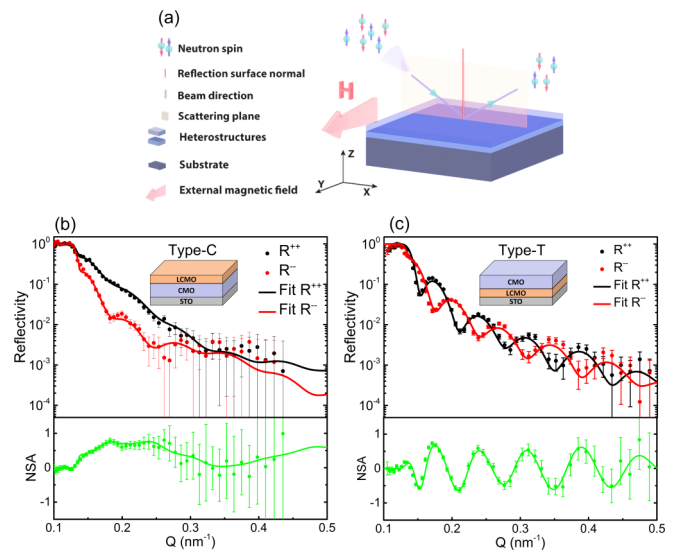


FIG. 6. (a) A schematic of polarized neutron reflectometry (PNR) experimental setup. The top panels of (b) and (c) display the PNR reflectivity data of the Type-C and Type-T heterostructures, respectively. The experimental data are represented by the data points with error bars, and the best fits are represented by lines which were obtained through a least-squares fitting procedure. The bottom panels of (b) and (c) display the corresponding Neutron spin asymmetry data which is calculated using $(R^{++} - R^{--})/(R^{++} + R^{--})$.

of a 1000 Oe external magnetic field, and a set of PNR measurements was performed at various magnetic fields starting from 1×10^4 Oe and reduced to -1×10^3 Oe. Only the data measured at 1×10^4 Oe are shown here, and the best fits (lines) to the experimental data (data points with error bars) were obtained using a least-squares fitting procedure. As shown in Figs. 6(b) and 6(c), the directly visualized difference in PNR results indicate there is distinct chemical and magnetic heterostructure stacking. The volume-averaged $M-H$ loop obtained following the same field history employed during PNR measurements is shown in Fig. S5 in the Supplemental Material [29], and an additional PNR dataset measured at 300 K is shown in Fig. S6 in the Supplemental Material [29] (see also Ref. [52] therein).

Figures 7(a) and 7(b) show the extracted nuclear SLD (NSLD) and magnetic SLD (MSLD) profiles of the heterostructures. The SLD profiles were extracted by fitting the R^{++} and R^{--} data and cross-checking against the XRR, cross-sectional TEM, and volume-averaged magnetometry results. More information about the fitting procedure is detailed in the Supplemental Material [29]. As shown in Fig. 7(a), for the Type-C heterostructure, the CMO layer displays a reduced NSLD that is 89% of the bulk value ($35.520 \times 10^{-5} \text{ nm}^{-2}$), while LCMO shows an enhanced NSLD that is 103% of the bulk value ($36.087 \times 10^{-5} \text{ nm}^{-2}$). The reduction of CMO NSLD is due to the oxygen vacancies in the relaxed CMO lattice; the oxygen vacancies cannot diffuse out of the CMO layer due to the presence of the LCMO overlayer [52]. While the reason for the slight increase in the NSLD of the LCMO layer is unclear, the increase is within the error resolution of the PNR technique. On the other hand, the NSLD profile of the Type-T heterostructure shown in Fig. 7(b) is distinctly

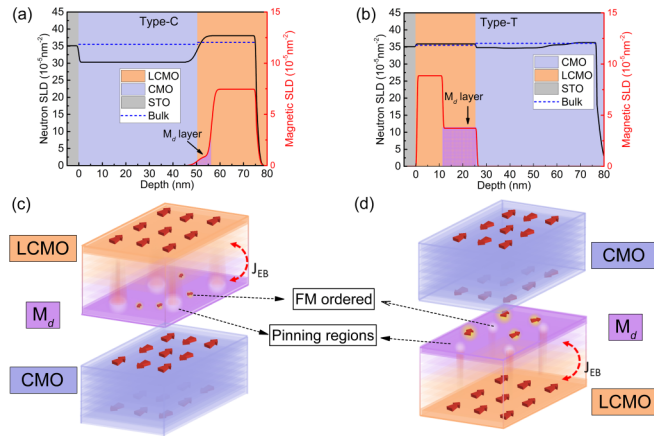


FIG. 7. The nuclear scattering length density (NSLD) and magnetic scattering length density (MSLD) model obtained from best fits to the polarized neutron reflectometry (PNR) data of the (a) Type-C and (b) Type-T heterostructures. The colored regions represent the different stacking sequences of the chemical layers within each heterostructure. The interfacial spin configurations of the heterostructures extracted from the analysis of the PNR data are depicted in (c) and (d) for the Type-C and Type-T heterostructures, respectively. A M_d layer forms at the interface between the nonfrustrated ferromagnetic (FM) $\text{La}_{0.7}\text{Ca}_{0.3}\text{MnO}_3$ (LCMO) layer and the antiferromagnetic (AFM) CaMnO_3 (CMO) layer in each heterostructure. The depicted magnetic state of each heterostructure is one where the critical cooling field is applied, giving rise to a maximum H_E .

different. In the Type-T heterostructure, the NSLD of the CMO layer gradually increases from 98 to 102% of its bulk value, while the LCMO layer shows 99% of the bulk value. The gradual increase in the NSLD of the CMO layer toward the heterostructure surface is due to the presence of oxygen vacancies in the relaxed CMO lattice which tend to diffuse into the atmosphere [52]. As for the MSLD profiles of the heterostructures, both show similar architectures consisting of magnetically depressed (M_d) regions and bulk like regions within the chemical LCMO layer, where the M_d layer is located at the LCMO/CMO interface in both heterostructures. Moreover, the magnetization (and thickness) of the M_d layer in Type-C and Type-T heterostructures are 32 emu/cm^3 (6 nm) and 130 emu/cm^3 (14.5 nm), respectively. For comparison, the bulk like part has a magnetization of 130 emu/cm^3 (19 nm) and 310 emu/cm^3 (11 nm) for Type-C and Type-T heterostructures, respectively. The fitted M_{average} for Type-C and Type-T heterostructures are 107 and 208 emu/cm^3 , respectively, which are in very good agreement with our magnetometry data (Fig. S5 in the Supplemental Material [29]). The PNR analysis suggests the existence of spin frustration at the LCMO/CMO interface, as evidenced by the presence of the M_d layer. The level of frustration is reflected in the magnetization of the M_d layer, whereby higher magnetization corresponds to a lower level of frustration and vice versa. The magnetization density ratio between the M_d layer and the bulk like layer [ratio = (area of the bulk like layer under the MSLD curve)/(area of the M_d layer under the MSLD curve)] are 0.09 and 0.55 for Type-C and Type-T heterostructures, respectively, which confirms this interpretation, and

it agrees with the volume-averaged magnetic measurements discussed earlier (i.e., the H_{cf} -dependent $M-H$ loops and $M-T$ curves).

A schematic representation of the interfacial spin structures of the heterostructures extracted from the analysis of the PNR data is shown in Figs. 7(c) and 7(d), for Type-C and Type-T heterostructures, respectively. In both heterostructures, an interfacial layer of frustrated spins arises from the competition between the AFM superexchange interaction of the CMO layer and the FM double-exchange interaction of the LCMO layer. Magnetic frustration at the LCMO/CMO interface results in a M_d layer which is treated as a combination of FM ordered regions (denoted by red arrows) and uncompensated, glassy spin regions which act as pinning sites (denoted by white areas). The spins within a single spin-cluster domain align parallel to each other, resulting in a net magnetic moment, while not all spin-cluster domains align colinearly with the field, resulting in the M_d layer possessing a net reduced magnetic moment (compared with the moment of the bulk like component of the LCMO layer). The EB interaction (J_{EB}) occurs at the magnetic interface in the LCMO layer, which is evidenced by the evolution of magnetization of the heterostructures when the magnetic field swept from 1×10^4 to -1×10^3 Oe, results shown in Fig. S7 in the Supplemental Material [29]. The M_d layer reaches zero magnetization before the spin reversal occurs in the bulk like LCMO layer and remains zero after the spin reversal has completed. This suggests that magnetic spin in the bulk like LCMO layer are pinned. Moreover, the strength of the J_{EB} depends on the detailed spin configurations present at the interface between the FM domains in the bulk like LCMO layer and the frustrated glassy spin domains. To this end, the phenomena observed in the H_{cf} data and their dependence on H_E and H_C can be explained as follows. When a small H_{cf} is applied, a large volume of the glassy spin phase exists in the M_d layer, resulting in a reduced magnetization in the bulk like component of the LCMO layer because the spins are not fully collinear with the field. The frustrated glassy spin domains randomly couple with the FM layer, creating an exchange anisotropy and a small negative H_E . As a result, there is no significant effect on the number of reversible spins, leading to a small increase in H_C . With increasing H_{cf} , more FM spins align with the cooling field, and more random exchange-coupled regions are induced, resulting in an enhancement of H_E . When H_{cf} surpasses a critical value that leads to the maximal H_E values, the density of frustrated glassy spin domains is reduced, and consequently, the region that enables the exchange coupling is reduced, resulting in a decreased H_E .

IV. CONCLUSIONS

In this paper, the correlation between the degree of spin frustration and the strength of EB is experimentally investigated in LCMO/CMO heterostructures with various atomic stacking sequences. Our results indicate that the degree of interfacial spin frustration can be efficiently controlled by manipulating the strain state through changes in the Mn e_g orbital at the chemical interface by alternating the stacking sequence of the LCMO/CMO heterostructures. We experimentally demonstrated that EB interaction occurs between the frustrated spin layer and the bulk like LCMO layer.

Furthermore, the frustrated spins are present within the LCMO layer at the interface to the CMO layer, which consist of glassy spin domains and small clusters of FM coupled spins. Multiple effective pinning regions randomly occupy the glassy spin domain of the frustrated layer M_d , wherein the density of pinning centers exhibits a dependence on temperature and field history. Strong exchange anisotropy, resulting from the coupling between FM spins and random distributed glassy spin pinning sites, presents within the LCMO layer, where a large H_E results by a high degree of spin frustration. A maximum H_E of -334 Oe is found for the highly frustrated Type-C heterostructure, while a maximum H_E of -15 Oe is observed for the less frustrated Type-T heterostructure. The achieved EB is one of the highest values in the complex oxide heterostructures. Finally, our findings establish a fundamental

principle, as well as a potential high-throughput device fabrication methodology, to realize tunable and high EB field spintronics through manipulating the strains in high-quality epitaxial complex oxide heterostructures. It creates the degree of interfacial frustration as another dimension to control the EB.

ACKNOWLEDGMENTS

The authors would like to thank the Australian Research Council No. DP190103661 for financial support. The authors acknowledge use of facilities in the Solid State & Elemental Analysis Unit at Mark Wainwright Analytical Centre. L.Q. was supported by the National Natural Science Foundation of China (Grant No. 11774044).

-
- [1] R. L. Stamps, Mechanisms for exchange bias, *J. Phys. D* **33**, R247 (2000).
- [2] V. Skumryev, S. Stoyanov, Y. Zhang, G. Hadjipanayis, D. Givord, and J. Nogués, Beating the superparamagnetic limit with exchange bias, *Nature (London)* **423**, 850 (2003).
- [3] J. Zhang, G. Zhou, Z. Yan, H. Ji, X. Li, Z. Quan, Y. Bai, and X. Xu, Interfacial ferromagnetic coupling and positive spontaneous exchange bias in $\text{SrFeO}_{3-x}/\text{La}_{0.7}\text{Sr}_{0.3}\text{MnO}_3$ bilayers, *ACS Appl. Mater. Interfaces* **11**, 26460 (2019).
- [4] M. Kiwi, J. Mejia-López, R. D. Portugal, and R. Ramirez, Positive exchange bias model: Fe/FeF_2 and Fe/MnF_2 bilayers, *Solid State Commun.* **116**, 315 (2000).
- [5] M. Ali, P. Adie, C. H. Marrows, D. Greig, B. J. Hickey, and R. L. Stamps, Exchange bias using a spin glass, *Nat. Mater.* **6**, 70 (2007).
- [6] K. Binder and A. P. Young, Spin glasses: experimental facts, theoretical concepts, and open questions, *Rev. Mod. Phys.* **58**, 801 (1986).
- [7] L. Balents, Spin liquids in frustrated magnets, *Nature (London)* **464**, 199 (2010).
- [8] R. F. Wang, C. Nisoli, R. S. Freitas, J. Li, W. McConville, B. J. Cooley, M. S. Lund, N. Samarth, C. Leighton, V. H. Crespi, and P. Schiffer, Artificial ‘spin ice’ in a geometrically frustrated lattice of nanoscale ferromagnetic islands, *Nature (London)* **439**, 303 (2006).
- [9] X. Z. Yu, Y. Onose, N. Kanazawa, J. H. Park, J. H. Han, Y. Matsui, N. Nagaosa, and Y. Tokura, Real-space observation of a two-dimensional skyrmion crystal, *Nature (London)* **465**, 901 (2010).
- [10] C. Nisoli, R. Moessner, and P. Schiffer, Colloquium: Artificial spin ice: designing and imaging magnetic frustration, *Rev. Mod. Phys.* **85**, 1473 (2013).
- [11] J. M. D. Coey, M. Venkatesan, and C. B. Fitzgerald, Donor impurity band exchange in dilute ferromagnetic oxides, *Nat. Mater.* **4**, 173 (2005).
- [12] V. Markovich, I. Fita, A. Wisniewski, G. Jung, D. Mogilyansky, R. Puzniak, L. Titelman, and G. Gorodetsky, Spin-glass-like properties of $\text{La}_{0.8}\text{Ca}_{0.2}\text{MnO}_3$ nanoparticles ensembles, *Phys. Rev. B* **81**, 134440 (2010).
- [13] J. F. Ding, O. I. Lebedev, S. Turner, Y. F. Tian, W. J. Hu, J. W. Seo, C. Panagopoulos, W. Prellier, G. Van Tendeloo, and T. Wu, Interfacial spin glass state and exchange bias in manganese bilayers with competing magnetic orders, *Phys. Rev. B* **87**, 054428 (2013).
- [14] X. Ding, B. Yang, H. Leng, J. H. Jang, J. Zhao, C. Zhang, S. Zhang, G. Cao, J. Zhang, R. Mishra, J. Yi, D. Qi, Z. Gai, X. Zu, S. Li, B. Huang, A. Borisevich, and L. Qiao, Crystal symmetry engineering in epitaxial perovskite superlattices, *Adv. Funct. Mater.* (2021) 2106466.
- [15] L. Qiao, J. H. Jang, D. J. Singh, Z. Gai, H. Xiao, A. Mehta, R. K. Vasudevan, A. Tselev, Z. Feng, H. Zhou, S. Li, W. Prellier, X. Zu, Z. Liu, A. Borisevich, A. P. Baddorf, and M. D. Biegalski, Dimensionality controlled octahedral symmetry-mismatch and functionalities in epitaxial $\text{LaCoO}_3/\text{SrTiO}_3$ heterostructures, *Nano Lett.* **15**, 4677 (2015).
- [16] A. Chen, Q. Wang, M. R. Fitzsimmons, E. Enriquez, M. Weigand, Z. Harrell, B. McFarland, X. Lü, P. Dowden, J. L. MacManus-Driscoll, D. Yarotski, and Q. Jia, Hidden interface driven exchange coupling in oxide heterostructures, *Adv. Mater.* **29**, 1700672 (2017).
- [17] L. Marín, L. A. Rodríguez, C. Magén, E. Snoeck, R. Arras, I. Lucas, L. Morellón, P. A. Algarabel, J. M. De Teresa, and M. R. Ibarra, Observation of the strain induced magnetic phase segregation in manganite thin films, *Nano Lett.* **15**, 492 (2015).
- [18] K. D. Usadel and U. Nowak, Exchange bias for a ferromagnetic film coupled to a spin glass, *Phys. Rev. B* **80**, 014418 (2009).
- [19] X. W. Li, Y. Lu, G. Q. Gong, G. Xiao, A. Gupta, P. Lecoeur, J. Z. Sun, Y. Y. Wang, and V. P. Dravid, Epitaxial $\text{La}_{0.67}\text{Sr}_{0.33}\text{MnO}_3$ magnetic tunnel junctions, *J. Appl. Phys.* **81**, 5509 (1997).
- [20] Y. Tokura and N. Nagaosa, Orbital physics in transition-metal oxides, *Science* **288**, 462 (2000).
- [21] X. Zhan, Z. Mao, X. Xu, X. Chen, and W. Kleemann, Spin disorder dependence of the exchange bias effect, *Phys. Rev. B* **86**, 020407 (2012).
- [22] F. K. Olsen, I. Hallsteinsen, E. Arenholz, T. Tybell, and E. Folven, Coexisting spin-flop coupling and exchange bias in $\text{LaFeO}_3/\text{La}_{0.7}\text{Sr}_{0.3}\text{MnO}_3$ heterostructures, *Phys. Rev. B* **99**, 134411 (2019).
- [23] Y. M. Liang, Z. J. Wang, Y. Bai, Y. J. Wu, X. K. Ning, X. F. Xiao, X. G. Zhao, W. Liu, and Z. D. Zhang, Interface-induced transition from a cluster glass state to a spin glass state in

- LaMnO₃/BiFeO₃ heterostructures, *J. Mater. Chem. C* **7**, 2376 (2019).
- [24] L. Qiao, K. H. L. Zhang, M. E. Bowden, T. Varga, V. Shutthanandan, R. Colby, Y. Du, B. Kabius, P. V. Sushko, M. D. Biegalski, and S. A. Chambers, The impacts of cation stoichiometry and substrate surface quality on nucleation, structure, defect formation, and intermixing in complex oxide heteroepitaxy—LaCrO₃ on SrTiO₃(001), *Adv. Funct. Mater.* **23**, 2953 (2013).
- [25] G. P. Felcher, R. O. Hilleke, R. K. Crawford, J. Haumann, R. Kleb, and G. Ostrowski, Polarized neutron reflectometer: a new instrument to measure magnetic depth profiles, *Rev. Sci. Instrum.* **58**, 609 (1987).
- [26] NIST Center for Neutron Research, Neutron scattering lengths and cross sections, <https://www.ncnr.nist.gov/resources/n-lengths/list.html>.
- [27] Y. M. Xiong, T. Chen, G. Y. Wang, X. H. Chen, X. Chen, and C. L. Chen, Raman spectra in epitaxial thin films of La_{1-x}Ca_xMnO₃ ($x = 0.33, 0.5$) grown on different substrates, *Phys. Rev. B* **70**, 094407 (2004).
- [28] F. Wang, B. J. Dong, Y. Q. Zhang, W. Liu, H. R. Zhang, Y. Bai, S. K. Li, T. Yang, J. R. Sun, Z. J. Wang, and Z. D. Zhang, Single orthorhombic *b* axis orientation and antiferromagnetic ordering type in multiferroic CaMnO₃ thin film with La_{0.67}Ca_{0.33}MnO₃ buffer layer, *Appl. Phys. Lett.* **111**, 122902 (2017).
- [29] See Supplemental Material at <http://link.aps.org/supplemental/10.1103/PhysRevB.104.174444> for high-resolution cross-sectional transmission electron microscopy, details of lattice parameters and layer thickness, magnetic memory effect experiment, temperature-dependent magnetization relaxation, temperature-dependent M-H loops following FC protocols, M-H loops of the heterostructures measured under identical conditions as the PNR, room temperature PNR, and PNR results of the evolution of magnetization as a function of magnetic field.
- [30] D. Imbrenda, D. Yang, H. Wang, A. R. Akbashev, L. Kasaei, B. A. Davidson, X. Wu, X. Xi, and J. E. Spanier, Surface- and strain-tuning of the optical dielectric function in epitaxially grown CaMnO₃, *Appl. Phys. Lett.* **108**, 082902 (2016).
- [31] L. Qiao, T. C. Droubay, M. E. Bowden, V. Shutthanandan, T. C. Kaspar, and S. A. Chambers, LaCrO₃ heteroepitaxy on SrTiO₃(001) by molecular beam epitaxy, *Appl. Phys. Lett.* **99**, 061904 (2011).
- [32] L. Qiao, T. C. Droubay, T. Varga, M. E. Bowden, V. Shutthanandan, Z. Zhu, T. C. Kaspar, and S. A. Chambers, Epitaxial growth, structure, and intermixing at the LaAlO₃/SrTiO₃ interface as the film stoichiometry is varied, *Phys. Rev. B* **83**, 085408 (2011).
- [33] S. A. Chambers, L. Qiao, T. C. Droubay, T. C. Kaspar, B. W. Arey, and P. V. Sushko, Band Alignment, Built-In Potential, and the Absence of Conductivity at the LaCrO₃/SrTiO₃ Heterojunction, *Phys. Rev. Lett.* **107**, 206802 (2011).
- [34] S. Zhang, J. Wang, S. Wen, M. Jiang, H. Xiao, X. Ding, N. Wang, M. Li, X. Zu, S. Li, C. Yam, B. Huang, and L. Qiao, Approaching Charge Separation Efficiency to Unity without Charge Recombination, *Phys. Rev. Lett.* **126**, 176401 (2021).
- [35] M. Ziese, H. C. Semmelhack, and K. H. Han, Strain-induced orbital ordering in thin La_{0.7}Ca_{0.3}MnO₃ films on SrTiO₃, *Phys. Rev. B* **68**, 134444 (2003).
- [36] E. Vincent and V. Dupuis, Spin glasses: experimental signatures and salient outcomes, in *Frustrated Materials and Ferrotic Glasses*, edited by T. Lookman and X. Ren (Springer International Publishing, Cham, 2018), p. 31.
- [37] Y. Konishi, Z. Fang, M. Izumi, T. Manako, M. Kasai, H. Kuwahara, M. Kawasaki, K. Terakura, and Y. Tokura, Orbital-state-mediated phase-control of manganites, *J. Phys. Soc. Jpn.* **68**, 3790 (1999).
- [38] D. Zheng, C. Jin, P. Li, L. Wang, L. Feng, W. Mi, and H. Bai, Orbital reconstruction enhanced exchange bias in La_{0.6}Sr_{0.4}MnO₃/orthorhombic YMnO₃ heterostructures, *Sci. Rep.* **6**, 24568 (2016).
- [39] C. Aruta, G. Ghiringhelli, A. Tebano, N. G. Boggio, N. B. Brookes, P. G. Medaglia, and G. Balestrino, Strain induced x-ray absorption linear dichroism in La_{0.7}Sr_{0.3}MnO₃ thin films, *Phys. Rev. B* **73**, 235121 (2006).
- [40] J. Garcia-Barriocanal, J. C. Cezar, F. Y. Bruno, P. Thakur, N. B. Brookes, C. Urfeld, A. Rivera-Calzada, S. R. Giblin, J. W. Taylor, J. A. Duffy, S. B. Dugdale, T. Nakamura, K. Kodama, C. Leon, S. Okamoto, and J. Santamaria, Spin and orbital Ti magnetism at LaMnO₃/SrTiO₃ interfaces, *Nat. Commun.* **1**, 82 (2010).
- [41] D. Sherrington and S. Kirkpatrick, Solvable Model of a Spin-Glass, *Phys. Rev. Lett.* **35**, 1792 (1975).
- [42] D. S. Fisher and D. A. Huse, Nonequilibrium dynamics of spin glasses, *Phys. Rev. B* **38**, 373 (1988).
- [43] M. K. Singh, R. S. Katiyar, W. Prellier, and J. F. Scott, The Almeida-Thouless line in BiFeO₃: Is bismuth ferrite a mean field spin glass?, *J. Phys.: Condens. Matter* **21**, 042202 (2008).
- [44] E. Vincent, J. P. Bouchaud, D. S. Dean, and J. Hammann, Aging in spin glasses as a random walk: effect of a magnetic field, *Phys. Rev. B* **52**, 1050 (1995).
- [45] C. P. Massen and J. P. K. Doye, Power-law distributions for the areas of the basins of attraction on a potential energy landscape, *Phys. Rev. E* **75**, 037101 (2007).
- [46] E. V. Colla, L. K. Chao, M. B. Weissman, and D. D. Viehland, Aging in a Relaxor Ferroelectric: Scaling and Memory Effects, *Phys. Rev. Lett.* **85**, 3033 (2000).
- [47] T. Kimura, Y. Tomioka, R. Kumai, Y. Okimoto, and Y. Tokura, Diffuse Phase Transition and Phase Separation in Cr-Doped Nd_{1/2}Ca_{1/2}MnO₃ A Relaxor Ferromagnet, *Phys. Rev. Lett.* **83**, 3940 (1999).
- [48] J. A. Mydosh, *Spin Glasses: An Experimental Introduction* (CRC Press, London, 2014).
- [49] P. Bag, P. R. Baral, and R. Nath, Cluster spin-glass behavior and memory effect in Cr_{0.5}Fe_{0.5}Ga, *Phys. Rev. B* **98**, 144436 (2018).
- [50] W. B. Rui, Y. Hu, A. Du, B. You, M. W. Xiao, W. Zhang, S. M. Zhou, and J. Du, Cooling field and temperature dependent exchange bias in spin glass/ferromagnet bilayers, *Sci. Rep.* **5**, 13640 (2015).
- [51] Y.-K. Tang, Y. Sun, and Z.-H. Cheng, Exchange bias associated with phase separation in the perovskite cobaltite La_{1-x}Sr_xCoO₃, *Phys. Rev. B* **73**, 174419 (2006).
- [52] R. U. Chandrasena, W. Yang, Q. Lei, M. U. Delgado-Jaime, K. D. Wijesekara, M. Gosalikhani, B. A. Davidson, E. Arenholz, K. Kobayashi, M. Kobata, F. M. F. de Groot, U. Aschauer, N. A. Spaldin, X. Xi, and A. X. Gray, Strain-engineered oxygen vacancies in CaMnO₃ thin films, *Nano Lett.* **17**, 794 (2017).